

On high-frequency radiation scattering sensitivity to surface roughness in particulate media

T. I. Zohdi¹

Received: 6 March 2016 / Revised: 9 May 2016 / Accepted: 25 May 2016
© OWZ 2016

Abstract This paper analyzes the sensitivity of high-frequency radiation scattering in particulate media, to particle surface roughness. Ray-tracing theory and computation are employed. Since the magnitude of the Poynting vector ray, the irradiance, is the appropriate quantity to be tracked, the behavior of the reflectance, which controls the ratio of the reflected and incident Poynting vector magnitudes, is of primary concern. The reflectance is a highly nonlinear function of the refractive indices and angle of incidence. The present work first addresses the relationship between a single scatterer's sensitivity to its surface roughness and then the response of a large number of scatterers to the surface roughness. The analysis indicates that, for a single scatterer, the *sensitivity of the response to roughness decreases, up to a point*, and then increases again, i.e., it is nonmonotone. However, for a system of multiple scatterers, this effect vanishes, due to multiple internal reflections which dominate the overall response characteristics. While it was relatively straightforward to compute the overall sensitivity of a single scattering body, for example a sphere, when multiple reflecting bodies are considered, numerical simulations are necessary because the reflected rays from one “rough” body will, in turn, be reflected to another “rough” body, etc. Examples are given for a system of randomly distributed scatterers.

Keywords Particles · Radiation · Scattering · Surface roughness

1 Introduction

A variety of techniques for determining the basic characteristics of particulate media utilize the scattering response to incident light or other high-frequency radiation beams. In particular, for granular flows, lasers can be directed into the system and a camera records and processes the scattered images. Approaches such as laser velocimetry use this approach to generate a sequence of images to characterize the dynamics of flows. The flow properties are obtained from consecutive images. Ray-tracing is a method that is employed to produce rapid approximate solutions to wave-equations for high-frequency/small-wavelength applications. Essentially, ray-tracing methods proceed by initially representing wave fronts by an array of discrete rays. *Thereafter, the problem becomes one of a purely geometric character*, where one tracks the changing trajectories of individual rays which are dictated by the Fresnel conditions (if a ray encounters a material interface). Ray-tracing methods are well-suited for computation of scattering in complex systems that are difficult to mesh/discretize, for example with a procedure such as the finite element method and, therefore, they are frequently employed by analysts in such situations. Thus, one component of interest in the present study is to develop a simple and fast computational tool, which captures the essential physics of incidence, absorption, and reflection, and then use it to perform parameter studies on how the roughness of the particles affect the overall response of a cloud to an incoming pulse of optical energy. Specifically, this paper primarily concentrates on the sensitivity of high-frequency radiation scattering responses of particulate systems to individual particle surface roughness. In particular, the sensitivity of systems comprising disordered aggregates of particles is addressed. Overall ray-dynamics, corresponding to flow of electromagnetic energy, is investigated. It is assumed that

✉ T. I. Zohdi
zohdi@berkeley.edu

¹ Department of Mechanical Engineering, University of California, 6195 Etcheverry Hall, Berkeley, CA 94720-1740, USA

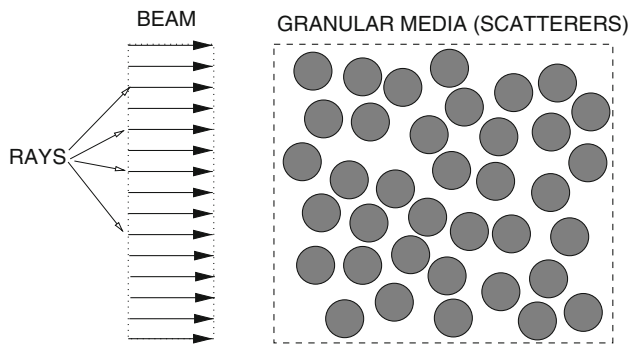


Fig. 1 The scattering system considered, comprising a beam, comprising multiple rays, incident on a collection of randomly distributed scatterers

the particles are at least an order of magnitude larger than the wavelength of the incident radiation, thus making geometrical optics and ray-tracing theory applicable (see Gross [16], Bohren and Huffman [2], Elmore and Heald [14], and van de Hulst [31]). We consider initially coherent beams (Fig. 1), composed of multiple collinear rays (forming a planar wave front), where each ray is a vector in the direction of the flow of electromagnetic energy.¹ Of particular interest is to describe the break-up of initially highly directional coherent beams, for example lasers, which do not spread out into multidirectional rays unless they encounter multiple scatterers. Ray-tracing is highly amenable to rapid large-scale computation needed to track the scattering of incident radiation beams, comprising of multiple rays, by multiple particles, and thus, it is the method of choice for the present analysis.

Remark In this work, we do not consider the problem of the dynamics on heat transfer of the dispersed particles within the cloud. For studies of the evolution of heat and the dynamics of the particles, we refer the reader to Zohdi [33,34,36–43]. This entails an analysis of the dynamics of particulate clouds and flows, related to granular flow models, as well as coupled fluid–particle interaction problems, which are found in Duran [13], Pöschel and Schwager [25], Onate et al. [22,23], Rojek et al. [28], Carbonell et al. [5], Labra and Onate [19], Avci and Wriggers [1], Leonardi et al. [21], Cante et al. [4], Rojek [27], Onate et al. [24], and Bolintineanu et al. [3].

2 Plane harmonic electromagnetic waves

Following a framework found in Zohdi [35,36,42,44] and Zohdi and Kuypers [45], we consider a beam of light incident upon a material interface which produces a reflected

wave and a transmitted (refracted) wave. The free space propagation of radiation can be described by a simplified form of Maxwell’s equations

$$\nabla \times \mathbf{E} = -\mu_0 \frac{\partial \mathbf{H}}{\partial t}, \quad \text{and} \quad \nabla \times \mathbf{H} = \epsilon_0 \frac{\partial \mathbf{E}}{\partial t}, \quad (2.1)$$

and

$$\nabla \cdot \mathbf{H} = 0, \quad \text{and} \quad \nabla \cdot \mathbf{E} = 0, \quad (2.2)$$

where \mathbf{E} is the electric field intensity, where \mathbf{H} is the magnetic flux intensity, where ϵ_0 is the permittivity, and where μ_0 is the permeability. Using standard vector identities, one can show that

$$\begin{aligned} \nabla \times (\nabla \times \mathbf{E}) &= -\mu_0 \epsilon_0 \frac{\partial^2 \mathbf{E}}{\partial t^2}, \quad \text{and} \\ \nabla \times (\nabla \times \mathbf{H}) &= -\mu_0 \epsilon_0 \frac{\partial^2 \mathbf{H}}{\partial t^2}, \end{aligned} \quad (2.3)$$

and that

$$\nabla^2 \mathbf{E} = \frac{1}{c^2} \frac{\partial^2 \mathbf{E}}{\partial t^2}, \quad \text{and} \quad \nabla^2 \mathbf{H} = \frac{1}{c^2} \frac{\partial^2 \mathbf{H}}{\partial t^2}, \quad (2.4)$$

where the speed of light is $c = \frac{1}{\sqrt{\epsilon_0 \mu_0}}$. Now consider the case of plane harmonic waves, for example of the form

$$\mathbf{E} = \mathbf{E}_0 \cos(\mathbf{k} \cdot \mathbf{r} - \omega t) \quad \text{and} \quad \mathbf{H} = \mathbf{H}_0 \cos(\mathbf{k} \cdot \mathbf{r} - \omega t), \quad (2.5)$$

where \mathbf{r} is an initial position vector to the wave front, \mathbf{k} is the direction of propagation, \mathbf{E}_0 is the amplitude of the electric field, and \mathbf{H}_0 is the amplitude of the magnetic field. For plane waves, $\mathbf{k} \cdot \mathbf{r} = \text{constant}$. We refer to the phase as $\phi = \mathbf{k} \cdot \mathbf{r} - \omega t$, and $\omega = \frac{2\pi}{\tau}$ as the angular frequency, where τ is the period. For “plane” waves, the wave front is a plane on which ϕ is constant, which is orthogonal to the direction of propagation, characterized by \mathbf{k} . In the case of harmonic waves, we have

$$\mathbf{k} \times \mathbf{E} = \mu_0 \omega \mathbf{H} \quad \text{and} \quad \mathbf{k} \times \mathbf{H} = -\epsilon_0 \omega \mathbf{E}, \quad (2.6)$$

and $\mathbf{k} \cdot \mathbf{E} = 0$ and $\mathbf{k} \cdot \mathbf{H} = 0$. The three vectors, \mathbf{k} , \mathbf{E} , and \mathbf{H} constitute a mutually orthogonal triad. The direction of ray propagation is given by $\frac{\mathbf{E} \times \mathbf{H}}{\|\mathbf{E} \times \mathbf{H}\|}$. Since the free space propagation velocity is given by $c = \frac{1}{\sqrt{\epsilon_0 \mu_0}}$ for an electromagnetic wave in a vacuum, and $v = \frac{1}{\sqrt{\epsilon \mu}}$ for electromagnetic waves in another medium, we can define the index of refraction as²

² All electromagnetic radiation travels at the speed of light in a vacuum, $c \approx 3 \times 10^8$ m/s. A more precise value, given by the National Bureau of Standards, is $c \approx 2.997924562 \times 10^8 \pm 1.1$ m/s. For visible light, the wavelength is between $3.8 \times 10^{-7} \leq \lambda \leq 7.2 \times 10^{-7}$ m.

¹ For isotropic media, the rays are parallel to the initial wave’s propagation vector (Fig. 1).

$$n \stackrel{\text{def}}{=} \frac{c}{v} = \sqrt{\frac{\epsilon\mu}{\epsilon_0\mu_0}} \tag{2.7}$$

2.1 High-frequency energy propagation

Electromagnetic waves traveling through space carry energy which flows in the direction of wave propagation. The energy per unit area per unit time flowing perpendicularly into a surface in free space is given by the Poynting vector $\mathbf{S} = \mathbf{E} \times \mathbf{H}$. Since at optical frequencies \mathbf{E} , \mathbf{H} , and \mathbf{S} oscillate rapidly, it is impractical to measure instantaneous values of \mathbf{S} directly. Now consider the harmonic representations in Eq. 2.5 which leads to

$$\mathbf{S} = \mathbf{E}_o \times \mathbf{H}_o \cos^2(\mathbf{k} \cdot \mathbf{r} - \omega t), \tag{2.8}$$

and consequently the average value over a longer time interval than the time scale of rapid random oscillation,

$$\langle \mathbf{S} \rangle_T = \mathbf{E}_o \times \mathbf{H}_o \langle \cos^2(\mathbf{k} \cdot \mathbf{r} - \omega t) \rangle_T = \frac{1}{2} \mathbf{E}_o \times \mathbf{H}_o. \tag{2.9}$$

We define the irradiance as

$$I \stackrel{\text{def}}{=} \langle \|\mathbf{S}\| \rangle_T = \frac{1}{2} \|\mathbf{E}_o \times \mathbf{H}_o\| = \frac{1}{2} \sqrt{\frac{\epsilon_o}{\mu_o}} \|\mathbf{E}_o\|^2. \tag{2.10}$$

Thus, the rate of flow of energy is proportional to the square of the amplitude of the electric field. Furthermore, in isotropic media, which we consider for the duration of the work, the direction of energy is in the direction of \mathbf{S} and in the same direction as \mathbf{k} . Since I is the energy per unit area per unit time, if we multiply by the ‘‘cross-sectional’’ area of the ray (a_r), we obtain the energy associated with the ray, denoted as $Ia_r = Ia_b/N_r$, where a_b is the cross-sectional area of a beam (comprising all of the rays) and N_r is the number of rays in the beam (Fig. 6).

2.2 Reflection and absorption of energy

One appeal of geometrical optics is that relatively elementary concepts are employed. For example, the *law of reflection* describes how radiation, such as light, is reflected from smooth surfaces (Fig. 2). The angle between the point of contact of a ray and the outward normal to the surface at that point is the angle of incidence (θ_i). The law of reflection states that the angle at which the radiation is reflected (θ_r) is the same as the angle of incidence ($\theta_i = \theta_r$) and that the incoming and outgoing rays lay in the same plane. The *law of refraction* states that, if the ray passes from one medium into a second one (with a different index of refraction), and, if the index of refraction of the second medium is less than that of the first, the angle the ray makes with the normal to the interface is

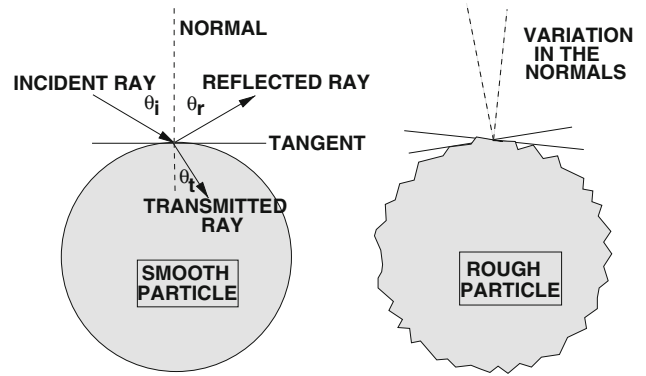


Fig. 2 The nomenclature for Fresnel’s equations for an incident ray that encounters an idealized smooth scattering particle and a ‘‘rough’’ particle with an uncertain surface

always less than the angle of incidence, and can be written as (the law of reflection)

$$n \stackrel{\text{def}}{=} \frac{v_{\text{vac}}}{v_{\text{med}}} = \frac{\sin \theta_i}{\sin \theta_t}, \tag{2.11}$$

where θ_t is the angle of the transmitted ray (Fig. 2). Throughout the paper we shall consider collections of particles ranging from perfectly reflecting types ($n \rightarrow \infty$), i.e., where the energy associated with a ray is entirely reflected (according to the law of reflection) to perfectly absorbing types ($n \rightarrow 1$), where a ray that makes contact with the particle surface is entirely absorbed and not re-emitted. For those particles with refractive indices existing between these extremes ($1 \leq n \leq \infty$), it is possible to go beyond a simple description of the direction of ray travel by employing the Fresnel equations, which are derived in the Appendix.

Henceforth, we consider a plane harmonic wave incident upon a plane boundary separating two different optical materials, which produces a reflected wave and a transmitted (refracted) wave (Fig. 2). The amount of incident electromagnetic energy (I_i) that is reflected (I_r) is given by the total reflectance

$$R \stackrel{\text{def}}{=} \frac{I_r}{I_i}, \tag{2.12}$$

where $0 \leq R \leq 1$ and where, for unpolarized radiation, such as natural light (see Appendix),

$$R = \frac{1}{2} \left(\left(\frac{\frac{\hat{n}^2}{\hat{\mu}} \cos \theta_i - (\hat{n}^2 - \sin^2 \theta_i)^{\frac{1}{2}}}{\frac{\hat{n}^2}{\hat{\mu}} \cos \theta_i + (\hat{n}^2 - \sin^2 \theta_i)^{\frac{1}{2}}} \right)^2 + \left(\frac{\cos \theta_i - \frac{1}{\hat{\mu}} (\hat{n}^2 - \sin^2 \theta_i)^{\frac{1}{2}}}{\cos \theta_i + \frac{1}{\hat{\mu}} (\hat{n}^2 - \sin^2 \theta_i)^{\frac{1}{2}}} \right)^2 \right), \tag{2.13}$$

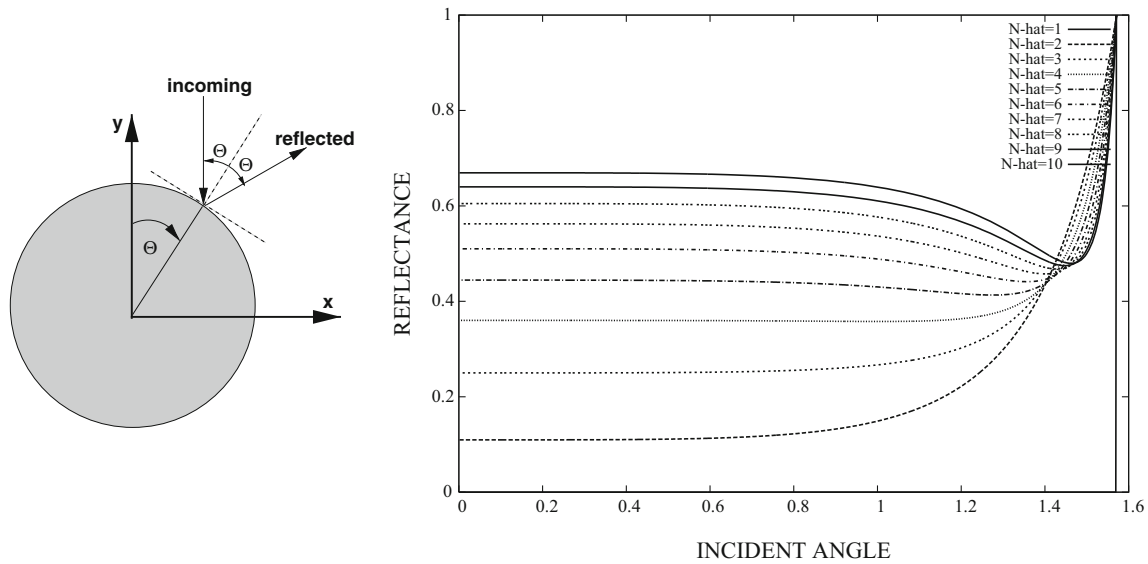


Fig. 3 Left a single scatterer. Right the reflectance (R) as a function of incident angle

where \hat{n} is the ratio of the refractive indices of the ambient (incident) medium (n_i) and transmitted particulate medium (n_t), $\hat{n} = n_t/n_i$, where $\hat{\mu}$ is the ratio of the magnetic permeabilities of the surrounding incident medium (μ_i) and transmitted particulate medium (μ_t), $\hat{\mu} = \mu_t/\mu_i$. For most materials, the magnetic permeability is, within experimental measurements, virtually the same, with a few notable exceptions such as concentrated magnetite, pyrrhotite, and titanomagnetite. Thus, for the remainder of the work, we shall take $\hat{\mu} = 1$, i.e., $\mu_o = \mu_i \approx \mu_t$.

Remark From this point forth, we assume that the ambient medium behaves as a vacuum. Accordingly, there are no energetic losses as the rays move through the surrounding medium. Furthermore, we assume that refracted rays which enter a particle are not re-emitted. The re-emission problem is quite complex, and involves multiple internal reflections, as well as conversion of optical energy into heat. It is important to note that multiple internal reflections and re-emission also leads to an immense growth in the number rays, which is beyond the scope of the present analysis. However, some of these issues have been addressed in Zohdi [35,36,42,44] and Zohdi and Kuypers [45].

3 Sensitivity of a single scatterer

Consider a single reflecting scatterer, with incident rays as shown in Fig. 3. For an individual ray, the sensitivity of the irradiance after a single reflection to surface roughness, a perturbation in the angle of incidence, can be represented as follows, from Eq. 2.12

$$\frac{\partial I_r}{\partial \theta} = \frac{\partial I_i}{\partial \theta} R + I_i \frac{\partial R}{\partial \theta}, \tag{3.1}$$

where for a single reflection $\frac{\partial I_i}{\partial \theta} = 0$, thus

$$\frac{\partial I_r}{\partial \theta} = I_i \frac{\partial R}{\partial \theta}. \tag{3.2}$$

For all rays at an incident angle between 0 and $\frac{\pi}{4}$, they are reflected with some positive y -component, i.e., “backwards” (back scatter). However, between $\frac{\pi}{4}$ and $\frac{\pi}{2}$, the rays are scattered with a negative y -component, i.e., forwards. Since the reflectance is the ratio of the amount of reflected energy (irradiance) to the incident energy, it is appropriate to consider the integrated reflectance over a quarter of a single scatterer, which indicates the total fraction of the irradiance reflected

$$\mathcal{I} \stackrel{\text{def}}{=} \frac{1}{\frac{\pi}{2}} \int_0^{\frac{\pi}{2}} R d\theta, \tag{3.3}$$

whose variation with \hat{n} is shown in Fig. 3. For a single scatterer, in the range tested ($1 \leq \hat{n} \leq 10$), the amount of energy reflected is a mildly nonlinear (quasilinear) function of \hat{n} and, thus, it should not be surprising that it is the same for an aggregate.³ Now consider the integral of the absolute value of the sensitivity to perturbations of the surface normal. The sensitivity of R to θ also represents the sensitivity to the outward surface normal, and thus represents the sensitivity to the surface roughness. Thus, locally, for surface roughness, $\frac{\partial R}{\partial \theta}$ is the correct quantity to track,

³ As $\hat{n} \rightarrow \infty$, the object becomes essentially “mirror-like.”

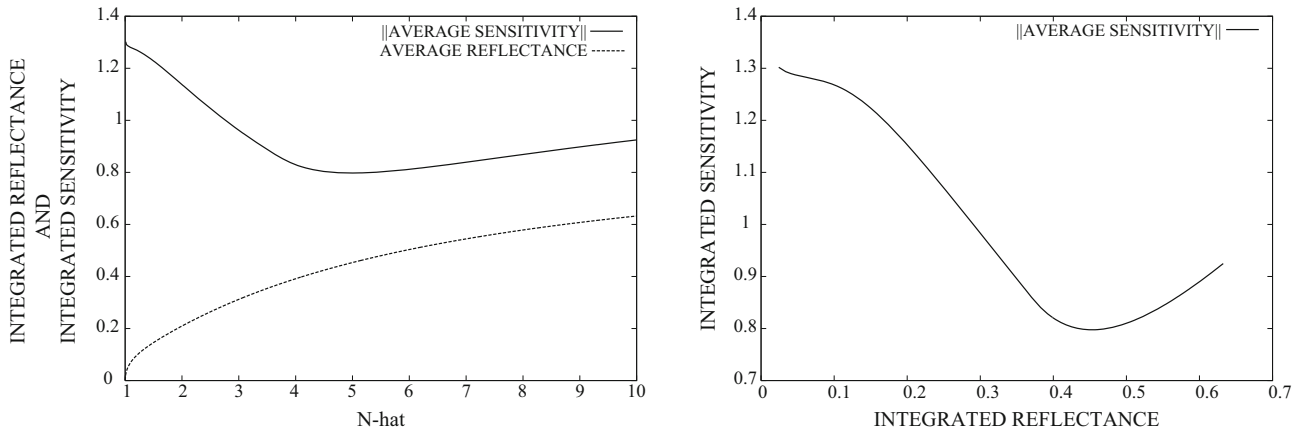


Fig. 4 The integrated reflectance (\mathcal{I}) and integrated sensitivity to surface perturbations $\frac{\partial \mathcal{I}}{\partial \theta}$ over a quarter of a single scatterer, which indicates the total fraction of the irradiance reflected. *Right* The integrated sensitivity versus the integrated reflectance

$$\frac{\partial \mathcal{I}}{\partial \theta} \stackrel{\text{def}}{=} \frac{1}{\frac{\pi}{2}} \int_0^{\frac{\pi}{2}} \left| \frac{\partial R}{\partial \theta} \right| d\theta. \quad (3.4)$$

As Fig. 4 indicates, the overall sensitivity of a single scatterer is a nonmonotone function of the ratio of refractive indices. Although this may appear surprisingly counterintuitive at first, the reflectance has a nonmonotone dependence on the angle of incidence, as Fig. 3 indicates, especially at higher values of \hat{n} , thus leading to the said overall nonmonotonicity of a single scatterer. However, as we shall illustrate in the next section, for multiple scatterers, the term in Eq. 3.1 representing the sensitivity to the incoming ray’s irradiance, $\frac{\partial I_i}{\partial \theta} R$, is no longer zero, due to multiple reflections, thus forcing the overall multiple scatterer system sensitivity to monotonically increase with increasing perturbations to the surface normals (“roughness”).

4 Multiple scatterers and multiple reflections

While it was relatively straightforward to compute the overall sensitivity of a single scattering body, for example a sphere, when multiple reflecting bodies were considered, numerical simulations are necessary because the reflected rays from one “rough” body would, in turn, be reflected to another “rough” body, etc.

4.1 Algorithmic solution procedure

The primary quantity of interest now is to characterize the difference between the response of the irradiance of a beam, encountering a collection of smooth particles and the response encountering a collection of rough particles after a given elapsed time T (Fig. 5), when all of the rays have exited the system (Fig. 6). This is characterized by the magnitude of the differences between the Poynting vector responses

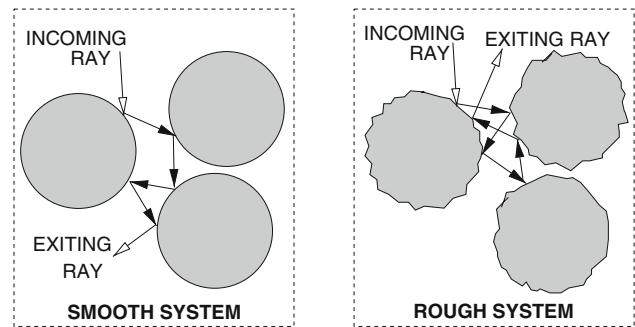


Fig. 5 One possible scenario when a ray encounters a rough system

between the smooth and rough collections of particles, motivating the following metric:

$$\mathcal{M} \stackrel{\text{def}}{=} \sqrt{\frac{\sum_{i=1}^{N_r} ((\tilde{S}_i - S_i) \cdot e_x)^2 + ((\tilde{S}_i - S_i) \cdot e_y)^2 + ((\tilde{S}_i - S_i) \cdot e_z)^2}{\sum_{i=1}^{N_r} ((S_i \cdot e_x)^2 + (S_i \cdot e_y)^2 + (S_i \cdot e_z)^2)}}, \quad (4.1)$$

where S_i is the Poynting vector of the i th ray propagating through the smooth particle system, \tilde{S}_i is the Poynting vector of the i th ray propagating through the rough particle system, e_x is the unit vector in the x -direction, e_y is the unit vector in the y -direction, and e_z is the unit vector in the z -direction.

The computational algorithm is as follows, starting at $t = 0$ and ending at $t = T$:

- (1) COMPUTE RAY REFLECTIONS (FRESNEL RELATIONS)
- (2) COMPUTE ABSORPTION BY PARTICLES
- (3) INCREMENT ALL RAY FRONT POSITIONS:
 $r_i(t + \Delta t) = r_i(t) + \Delta t v_i(t), \quad i = 1, \dots, \text{RAYS}$
- (4) GO TO (1) AND REPEAT WITH $(t = t + \Delta t)$

(4.2)

The time step size Δt is dictated by the size of the particles. A somewhat ad hoc approach is to scale the time step size according to $\Delta t \propto \frac{\xi b}{\|\mathbf{v}\|}$, where b is the radius of the particles, $\|\mathbf{v}\|$ is the magnitude of the velocity of the rays, and ξ is a scaling factor, typically $0.05 \leq \xi \leq 0.1$.

Remark It is important to recognize that one can describe the aggregate ray behavior in an even more detailed manner via higher moment distributions of rays, for example employing the skewness, kurtosis.

4.2 Parametrization of the scatterers

We considered a group of N_p randomly dispersed spherical particles, of equal size, in a cubical domain of dimensions, $D \times D \times D$, $D = 10^{-3}$ m. The particle size and volume fraction were determined by a particle/sample size ratio, which was defined via a subvolume size $V \stackrel{\text{def}}{=} \frac{D \times D \times D}{N_p}$, where N_p was the number of particles in the entire cube. The ratio between the radius (b) and the subvolume was denoted by $\mathcal{L} \stackrel{\text{def}}{=} \frac{b}{V^{1/3}}$. The volume fraction occupied by the particles consequently can be written as $v_p \stackrel{\text{def}}{=} \frac{4\pi\mathcal{L}^3}{3}$. Thus, the total volume occupied by the particles,⁴ denoted ζ , can be written as $\zeta = v_p N_p V$. We used $N_p = 1000$ particles and $N_r = 1600$ rays, arranged in a square 40×40 pattern (Fig. 6). This system provided stable results, i.e., increasing the number of rays and/or the number of particles beyond these levels resulted in negligibly different overall system responses. The irradiance beam parameter was set to $I_o = \|\mathbf{I}(0)\|$, which is the magnitude of the initial irradiance at time $t = 0$. The irradiance for each ray was calculated as $I a_b / N_r$, where $N_r = 40 \times 40 = 1600$ was the number of rays in the beam and $a_b = 10^{-3} \text{ m} \times 10^{-3} \text{ m} = 10^{-6} \text{ m}^2$ was the cross-sectional area of the beam.⁵

4.3 Results

The simulations were run until the rays completely exited the domain, which corresponded to a time scale on the order of $\frac{3 \times 10^{-3} \text{ m}}{c}$, where c is the speed of light. The initial velocity vector for all of the initially colinear rays comprising the beam was $\mathbf{v} = (c, 0, 0)$. Table 1 illustrates the response sensitivity of the same configuration of particles for a given

roughness equivalent to noise of 10% in the surface normals. As opposed to the trend for the single scatterer, the overall sensitivity is monotonically increasing \hat{n} , approximately according to the sublinear (curve-fit) relation

$$\mathcal{M} = 0.7946 \hat{n}^{0.007113}. \tag{4.4}$$

As indicated in Table 1, the rays undergo multiple reflections, and thus $\frac{\partial I_i}{\partial \theta} R \gg I_i \frac{\partial R}{\partial \theta}$, and any nonmonotonicity produced by $I_i \frac{\partial R}{\partial \theta}$ is dwarfed by $\frac{\partial I_i}{\partial \theta} R$. Additional parameter studies were performed where the particle length scale was varied between $0.25 \leq \mathcal{L} \leq 0.375$, while the relative refractive index ratio was varied between $2 \leq \hat{n} \leq 100$, with the results being qualitatively the same.

Remark We repeated refined the “ray grid” up to 100×100 rays (10,000 total) and found no significant difference compared to the 40×40 result. Therefore, we consider the responses to be, for all practical purposes, independent of the ray-grid density. Also, the average number of reflections for the smooth surface case was 2.91, while for the rough case it was 22.38. The large number of internal reflections for the rough case can be attributed to rays becoming trapped within the microstructure and “bouncing” back and forth between the rough surfaces. While this “bouncing” does occur for smooth cases, it does not happen with such severity as in the rough surface case.

5 Concluding remarks

In summary, this work developed a discrete-ray/discrete-particle model to allow the study of the propagation of optical energy through a cloud of randomly dispersed rough particles. The simplified model captures the primary effects, namely, reflection and absorption of optical energy via: (1) a discrete element representation of the particle system, (2) a discretization of a concentrated optical beam into rays, and (3) a discrete-ray tracking algorithm is developed to track the propagation of rays. *The simulations take on the order of 2 min on a laptop.* With this tool, the sensitivity of high-frequency electromagnetic scattering in particulate suspensions, to the particle surface roughness was studied. Ray-tracing theory was employed, and was justified due to the size of the scatterers relative to the wavelength of the incident radiation. The behavior of the reflectance, which controls the ratio of the reflected and incident Poynting vector magnitudes is a highly nonlinear function of the refractive indices and angle of incidence. This work addressed the relationship between a single scatterer’s sensitivity to its surface roughness and then the sensitivity of the response of a large number of scatterers. As was shown, for a single scatterer the *sensitivity of the response to roughness decreases, up to a*

⁴ For example, if one were to arrange the particles in a regular periodic manner, then at the length scale ratio of $\mathcal{L} = 0.25$ the distance between the centers of the particle become four particle radii. In theoretical works, it is often stated that the critical separation distance between particles is approximately three radii to be sufficient to treat the particles as independent scatterers, and simply to sum the effects of the individual scatterers to compute the overall response of the aggregate.

⁵ Because of the normalized structure of the \mathcal{M} -metric, it is insensitive to the initial magnitude of I_o .

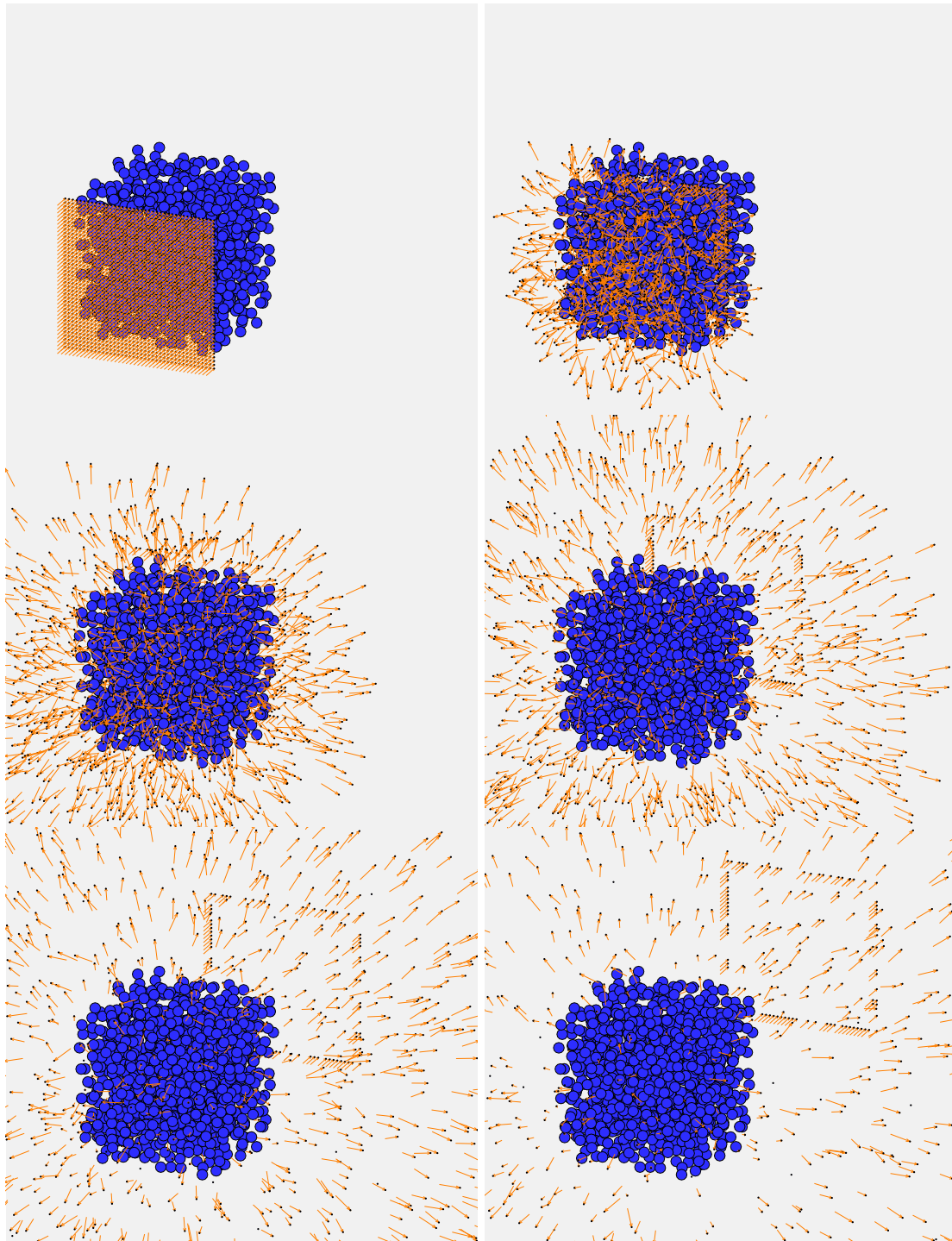


Fig. 6 Starting from *left to right* and *top to bottom*, the progressive movement of rays comprising a beam ($\mathcal{L} = 0.325$ and $\hat{n} = 4$), for a “rough” set of particles. The length of the vectors indicate the irradiance

point, and then increases again, i.e., it is nonmonotone. However, for many scatterers, this effect vanishes, due to multiple internal system reflections between scatterers, which dominate the overall response characteristics. As mentioned in the beginning of the paper, the regimes of validity of such a

model are where the particle scatterers and surface features are larger than visible light rays: $3.8 \times 10^{-7} \leq \lambda \leq 7.2 \times 10^{-7}$ m. The particles in this analysis were assumed to possess diameters larger than approximately 10^{-5} m ($10 \mu\text{m}$). For systems with particulates smaller than this, one can interpret

Table 1 $\mathcal{L} = 0.325$

\hat{n}	\mathcal{M}
2	0.09725
4	0.28888
8	0.41645
16	0.53994

The response sensitivity to a 40×40 ray mesh for 1000 randomly dispersed scatterers for increasing \hat{n} after a sufficiently long time $t = T$, allowing all of the rays to have exited the scattering system ($\mathcal{L} = 0.325$)

the results of the model in a qualitative manner, although the range of applicability is not limited to visible frequencies. Other high-frequency applications where the developed model can be employed include UV-rays, X-rays, gamma rays, and correspondingly smaller particle scatterer sizes, such as (a) regimes where the scatterers and surface features are larger than ultraviolet rays ($10^{-9} \leq \lambda \leq 10^{-8}$ m), (b) regimes where the scatterers and surface features are larger than X-rays ($10^{-11} \leq \lambda \leq 10^{-9}$ m), and (c) regimes where the scatterers and surface features are larger than gamma rays ($10^{-12} \leq \lambda \leq 10^{-11}$ m).

In closing, we note that this work has been partially motivated by the advances, within the last few decades, in the development of optically based imaging technologies, such as Light Detection And Ranging (LIDAR)-type technologies. LIDAR is a technique by which a target is illuminated with a laser and the reflected light is analyzed.⁶ LIDAR was developed in the 1960s and combines laser focusing with radar-like technology for calculating distances by measuring time to for signal return. LIDAR has become a relatively standard tool in the atmospheric sciences, ranging from remote sensing, airborne laser mapping, and cloud measurement, and has been extended to a variety of applications in engineering and science. For reviews, we refer the reader to Ring [26], Cracknell and Hayes [7], Goyer and Watson [15], and Medina et al. [20]. Recently, there have also been efforts in developing particulate penetrating/filtering LIDAR (Trickey et al. [30]).⁷ It has also started finding usage in the characterization of intentionally released particulate clouds, such as obscurants, and is a subject currently being investigated by the author (Zohdi [44]).

⁶ Usually, LIDAR uses high-frequency ultraviolet, visible and near infrared light.

⁷ Generally, LIDAR bears some similarity with particle image velocimetry technologies.

Compliance with ethical standards

Conflicts of interest The author declares that he has no conflicts of interest for this research.

Appendix: Generalized Fresnel relations

Following a generalization of the Fresnel relations for unequal magnetic permeabilities in Zohdi [35,36] and Zohdi and Kuypers [45], we consider a plane harmonic wave incident upon a plane boundary separating two different optical materials, which produces a reflected wave and a transmitted (refracted) wave (Fig. 2). Two cases for the electric field vector are considered: (1) electric field vectors that are parallel (\parallel) to the plane of incidence and (2) electric field vectors that are perpendicular (\perp) to the plane of incidence. In either case, the tangential components of the electric and magnetic fields are required to be continuous across the interface. Consider case (1). We have the following general vectorial representations

$$E_{\parallel} = E_{\parallel} \cos(\mathbf{k} \cdot \mathbf{r} - \omega t) \mathbf{e}_1 \quad \text{and} \quad \mathbf{H}_{\parallel} = H_{\parallel} \cos(\mathbf{k} \cdot \mathbf{r} - \omega t) \mathbf{e}_2, \tag{5.1}$$

where \mathbf{e}_1 and \mathbf{e}_2 are orthogonal to the propagation direction \mathbf{k} . By employing the law of refraction ($n_i \sin \theta_i = n_t \sin \theta_t$), we obtain the following conditions relating the incident, reflected and transmitted components of the electric field quantities

$$E_{\parallel i} \cos \theta_i - E_{\parallel r} \cos \theta_r = E_{\parallel t} \cos \theta_t \quad \text{and} \quad H_{\perp i} + H_{\perp r} = H_{\perp t}. \tag{5.2}$$

Since, for plane harmonic waves, the magnetic and electric field amplitudes are related by $H = \frac{E}{v\mu}$, we have

$$E_{\parallel i} + E_{\parallel r} = \frac{\mu_i v_i}{\mu_t v_t} E_{\parallel t} = \frac{\mu_i n_t}{\mu_t n_i} E_{\parallel t} \stackrel{\text{def}}{=} \hat{\mu} E_{\parallel t}, \tag{5.3}$$

where $\hat{\mu} \stackrel{\text{def}}{=} \frac{\mu_t}{\mu_i}$, $\hat{n} \stackrel{\text{def}}{=} \frac{n_t}{n_i}$ and where v_i , v_r and v_t are the values of the velocity in the incident, reflected and transmitted directions.⁸ By again employing the law of refraction, we obtain the Fresnel reflection and transmission coefficients, generalized for the case of unequal magnetic permeabilities

$$r_{\parallel} = \frac{E_{\parallel r}}{E_{\parallel i}} = \frac{\hat{\mu} \cos \theta_i - \cos \theta_t}{\hat{\mu} \cos \theta_i + \cos \theta_t} \quad \text{and} \quad t_{\parallel} = \frac{E_{\parallel t}}{E_{\parallel i}} = \frac{2 \cos \theta_i}{\cos \theta_t + \hat{\mu} \cos \theta_i}. \tag{5.4}$$

⁸ Throughout the analysis we assume that $\hat{n} \geq 1$.

Following the same procedure for case (2), where the components of \mathbf{E} are perpendicular to the plane of incidence, we have

$$r_{\perp} = \frac{E_{\perp r}}{E_{\perp i}} = \frac{\cos \theta_i - \frac{\hat{n}}{\hat{\mu}} \cos \theta_i}{\cos \theta_i + \frac{\hat{n}}{\hat{\mu}} \cos \theta_i} \quad \text{and}$$

$$t_{\perp} = \frac{E_{\perp t}}{E_{\perp i}} = \frac{2 \cos \theta_i}{\cos \theta_i + \frac{\hat{n}}{\hat{\mu}} \cos \theta_i}. \quad (5.5)$$

Our primary interest is in the reflections. We define the reflectances as

$$R_{\parallel} \stackrel{\text{def}}{=} r_{\parallel}^2 \quad \text{and} \quad R_{\perp} \stackrel{\text{def}}{=} r_{\perp}^2. \quad (5.6)$$

Particularly convenient forms for the reflections are

$$r_{\parallel} = \frac{\frac{\hat{n}^2}{\hat{\mu}} \cos \theta_i - (\hat{n}^2 - \sin^2 \theta_i)^{\frac{1}{2}}}{\frac{\hat{n}^2}{\hat{\mu}} \cos \theta_i + (\hat{n}^2 - \sin^2 \theta_i)^{\frac{1}{2}}} \quad \text{and}$$

$$r_{\perp} = \frac{\cos \theta_i - \frac{1}{\hat{\mu}} (\hat{n}^2 - \sin^2 \theta_i)^{\frac{1}{2}}}{\cos \theta_i + \frac{1}{\hat{\mu}} (\hat{n}^2 - \sin^2 \theta_i)^{\frac{1}{2}}}. \quad (5.7)$$

Thus, the total energy reflected can be characterized by

$$R \stackrel{\text{def}}{=} \left(\frac{E_r}{E_i} \right)^2 = \frac{E_{\perp r}^2 + E_{\parallel r}^2}{E_i^2} = \frac{I_{\parallel r} + I_{\perp r}}{I_i}. \quad (5.8)$$

If the resultant plane of oscillation of the (polarized) wave makes an angle of γ_i with the plane of incidence, then

$$E_{\parallel i} = E_i \cos \gamma_i \quad \text{and} \quad E_{\perp i} = E_i \sin \gamma_i, \quad (5.9)$$

and it follows from the previous definition of I that

$$I_{\parallel i} = I_i \cos^2 \gamma_i \quad \text{and} \quad I_{\perp i} = I_i \sin^2 \gamma_i. \quad (5.10)$$

Substituting these expression back into the expressions for the reflectances yields

$$R = \frac{I_{\parallel r}}{I_i} \cos^2 \gamma_i + \frac{I_{\perp r}}{I_i} \sin^2 \gamma_i = R_{\parallel} \cos^2 \gamma_i + R_{\perp} \sin^2 \gamma_i. \quad (5.11)$$

For natural or unpolarized radiation, the angle γ_i varies rapidly in a random manner, as does the field amplitude. Thus, since

$$\left\langle \cos^2 \gamma_i(t) \right\rangle_{\mathcal{T}} = \frac{1}{2} \quad \text{and} \quad \left\langle \sin^2 \gamma_i(t) \right\rangle_{\mathcal{T}} = \frac{1}{2}, \quad (5.12)$$

and therefore for natural radiation

$$I_{\parallel i} = \frac{I_i}{2} \quad \text{and} \quad I_{\perp i} = \frac{I_i}{2}. \quad (5.13)$$

and therefore

$$r_{\parallel}^2 = \left(\frac{E_{\parallel r}}{E_{\parallel i}} \right)^2 = \frac{I_{\parallel r}}{I_{\parallel i}} \quad \text{and} \quad r_{\perp}^2 = \left(\frac{E_{\perp r}}{E_{\perp i}} \right)^2 = \frac{I_{\perp r}}{I_{\perp i}}. \quad (5.14)$$

Thus, the total reflectance becomes

$$R = \frac{1}{2} (R_{\parallel} + R_{\perp}) = \frac{1}{2} (r_{\parallel}^2 + r_{\perp}^2), \quad (5.15)$$

where $0 \leq R \leq 1$. For the cases where $\sin \theta_t = \frac{\sin \theta_i}{\hat{n}} > 1$, one may rewrite reflection relations as

$$r_{\parallel} = \frac{\frac{\hat{n}^2}{\hat{\mu}} \cos \theta_i - j(\sin^2 \theta_i - \hat{n}^2)^{\frac{1}{2}}}{\frac{\hat{n}^2}{\hat{\mu}} \cos \theta_i + j(\sin^2 \theta_i - \hat{n}^2)^{\frac{1}{2}}} \quad \text{and}$$

$$r_{\perp} = \frac{\cos \theta_i - \frac{1}{\hat{\mu}} j(\sin^2 \theta_i - \hat{n}^2)^{\frac{1}{2}}}{\cos \theta_i + \frac{1}{\hat{\mu}} j(\sin^2 \theta_i - \hat{n}^2)^{\frac{1}{2}}}, \quad (5.16)$$

where, $j = \sqrt{-1}$, and in this complex case⁹

$$R_{\parallel} \stackrel{\text{def}}{=} r_{\parallel} \bar{r}_{\parallel} = 1, \quad \text{and} \quad R_{\perp} \stackrel{\text{def}}{=} r_{\perp} \bar{r}_{\perp} = 1, \quad (5.17)$$

where \bar{r}_{\parallel} and \bar{r}_{\perp} are complex conjugates. Thus, for angles above the critical angle θ_i^* , all of the energy is reflected. Notice that as $\hat{n} \rightarrow 1$ we have complete absorption, while as $\hat{n} \rightarrow \infty$ we have complete reflection. The total amount of absorbed power by the particles is $(1 - R)I_i$. Thermal (infrared) coupling effects, which are outside of the scope of this paper, have been accounted for in Zohdi [35,36] and Zohdi and Kuypers [45].

In order to understand the dependency of the results on \hat{n} , recall the fundamental relation for reflectance

$$R = \frac{1}{2} \left(\left(\frac{\frac{\hat{n}^2}{\hat{\mu}} \cos \theta_i - (\hat{n}^2 - \sin^2 \theta_i)^{\frac{1}{2}}}{\frac{\hat{n}^2}{\hat{\mu}} \cos \theta_i + (\hat{n}^2 - \sin^2 \theta_i)^{\frac{1}{2}}} \right)^2 + \left(\frac{\cos \theta_i - \frac{1}{\hat{\mu}} (\hat{n}^2 - \sin^2 \theta_i)^{\frac{1}{2}}}{\cos \theta_i + \frac{1}{\hat{\mu}} (\hat{n}^2 - \sin^2 \theta_i)^{\frac{1}{2}}} \right)^2 \right), \quad (5.18)$$

whose variation as a function of the angle θ_i is depicted in Fig. 3. For all but $\hat{n} = 2$, is there discernible nonmonotone behavior. The nonmonotone behavior is slight for $\hat{n} = 4$, but nonetheless present. Clearly, as $\hat{n} \rightarrow \infty$, $R \rightarrow 1$, no matter what the angle of incidence's value. Also, as $\hat{n} \rightarrow 1$, provided that $\hat{\mu} = 1$, $R \rightarrow 0$, i.e., all incident energy is absorbed. With increasing \hat{n} , the angle for minimum reflectance grows larger.

⁹ The limiting case $\frac{\sin \theta_i^*}{\hat{n}} = 1$, is the critical angle (θ_i^*) case.

References

1. Avci B, Wriggers P (2012) A DEM-FEM coupling approach for the direct numerical simulation of 3D particulate flows. *J Appl Mech* 79(1–7):010901
2. Bohren C, Huffman D (1998) Absorption and scattering of light by small particles. Wiley Science Paperback Series, Weinheim
3. Bolintineanu DS, Grest GS, Lechman JB, Pierce F, Plimpton SJ, Schunk PR (2014) Particle dynamics modeling methods for colloid suspensions. *Comput Part Mech* 1(3):321–356
4. Cante J, Davalos C, Hernandez JA, Oliver J, Jonsen P, Gustafsson G, Haggblad HA (2014) PFEM-based modeling of industrial granular flows. *Comput Part Mech* 1(1):47–70
5. Carbonell JM, Onate E, Suarez B (2010) Modeling of ground excavation with the particle finite element method. *J Eng Mech ASCE* 136:455–463
6. Cerveny V, Molotkov IA, Psencik I (1977) Ray methods in seismology. Univerzita Karlova, Praha
7. Cracknell AP, Hayes L (2007) Introduction to remote sensing, vol 2. Taylor and Francis, London. ISBN 0-8493-9255-1. OCLC 70765252
8. Donev A, Cisse I, Sachs D, Variano EA, Stillinger F, Connelly R, Torquato S, Chaikin P (2004a) Improving the density of jammed disordered packings using ellipsoids. *Science* 303:990–993
9. Donev A, Stillinger FH, Chaikin PM, Torquato S (2004b) Unusually dense crystal ellipsoid packings. *Phys Rev Lett* 92:255506
10. Donev A, Torquato S, Stillinger F (2005a) Neighbor list collision-driven molecular dynamics simulation for nonspherical hard particles—I. Algorithmic details. *J Comput Phys* 202:737
11. Donev A, Torquato S, Stillinger F (2005b) Neighbor list collision-driven molecular dynamics simulation for nonspherical hard particles—II. Application to ellipses and ellipsoids. *J Comput Phys* 202:765
12. Donev A, Torquato S, Stillinger FH (2005c) Pair correlation function characteristics of nearly jammed disordered and ordered hard-sphere packings. *Phys Rev E* 71:011105
13. Duran J (1997) Sands, powders and grains. An introduction to the physics of Granular Matter. Springer, New York
14. Elmore WC, Heald MA (1985) Physics of waves. Dover Publications, New York (re-issue)
15. Goyer GG, Watson R (1963) The laser and its application to meteorology. *Bull Am Meteorol Soc* 44(9):564–575 [568]
16. Gross H (2005) In: Gross H (ed) Handbook of optical systems. Fundamental of technical optics. Wiley-VCH, Weinheim
17. Kansa A, Torquato S, Stillinger F (2002) Diversity of order and densities in jammed hard-particle packings. *Phys Rev E* 66:041109
18. Jackson JD (1998) Classical electrodynamics, 3rd edn. Wiley, New York
19. Labra C, Onate E (2009) High-density sphere packing for discrete element method simulations. *Commun Numer Methods Eng* 25(7):837–849
20. Medina A, Gaya F, Pozo F (2006) Compact laser radar and three-dimensional camera. *J Opt Soc Am A* 23:800–805
21. Leonardi A, Wittel FK, Mendoza M, Herrmann HJ (2014) Coupled DEM-LBM method for the free-surface simulation of heterogeneous suspensions. *Comput Part Mech* 1(1):3–13
22. Onate E, Idelsohn SR, Celigueta MA, Rossi R (2008) Advances in the particle finite element method for the analysis of fluid–multibody interaction and bed erosion in free surface flows. *Comput Methods Appl Mech Eng* 197(19–20):1777–1800
23. Onate E, Celigueta MA, Idelsohn SR, Salazar F, Suarez B (2011) Possibilities of the particle finite element method for fluid–soil–structure interaction problems. *Comput Mech* 48:307–318
24. Onate E, Celigueta MA, Latorre S, Casas G, Rossi R, Rojek J (2014) Lagrangian analysis of multiscale particulate flows with the particle finite element method. *Comput Part Mech* 1(1):85–102
25. Pöschel T, Schwager T (2004) Computational granular dynamics. Springer, New York
26. Ring J (1963) The laser in astronomy. *N Sci* June:672–673
27. Rojek J (2014) Discrete element thermomechanical modelling of rock cutting with valuation of tool wear. *Comput Part Mech* 1(1):71–84
28. Rojek J, Labra C, Su O, Onate E (2012) Comparative study of different discrete element models and evaluation of equivalent micromechanical parameters. *Int J Solids Struct* 49:1497–1517. doi:10.1016/j.ijsolstr.2012.02.032
29. Torquato S (2002) Random heterogeneous materials: microstructure & macroscopic properties. Springer, New York
30. Trickey E, Church P, Cao X (2013) Characterization of the OPAL obscurant penetrating LiDAR in various degraded visual environments. In: Proceedings of SPIE 8737, degraded visual environments: enhanced, synthetic, and external vision solutions 2013, 87370E, 16 May 2013. doi:10.1117/12.2015259
31. van de Hulst HC (1981) Light scattering by small particles. Dover Publications, New York (re-issue)
32. Widom B (1966) Random sequential addition of hard spheres to a volume. *J Chem Phys* 44:3888–3894
33. Zohdi TI (2004) A computational framework for agglomeration in thermo-chemically reacting granular flows. *Proc R Soc* 460(2052):3421–3445
34. Zohdi TI (2005) Charge-induced clustering in multifield particulate flow. *Int J Numer Methods Eng* 62(7):870–898
35. Zohdi TI (2006a) On the optical thickness of disordered particulate media. *Mech Mater* 38:969–981
36. Zohdi TI (2006b) Computation of the coupled thermo-optical scattering properties of random particulate systems. *Comput Methods Appl Mech Eng* 195:5813–5830
37. Zohdi TI (2007) Computation of strongly coupled multifield interaction in particle-fluid systems. *Comput Methods Appl Mech Eng* 196:3927–3950
38. Zohdi TI (2010) On the dynamics of charged electromagnetic particulate jets. *Arch Comput Methods Eng* 17(2):109–135
39. Zohdi TI (2012a) Electromagnetic properties of multiphase dielectrics. A primer on modeling, theory and computation. Springer, New York
40. Zohdi TI (2012b) Dynamics of charged particulate systems. Modeling, theory and computation. Springer, New York
41. Zohdi TI (2013a) Numerical simulation of charged particulate cluster-droplet impact on electrified surfaces. *J Comput Phys* 233:509–526
42. Zohdi TI (2013b) Rapid simulation of laser processing of discrete particulate materials. *Arch Comput Methods Eng* 20:309–325
43. Zohdi T (2014) Embedded electromagnetically sensitive particle motion in functionalized fluids. *Comput Part Mech* 1(1):27–45
44. Zohdi TI (2015) A computational modelling framework for high-frequency particulate obscurant cloud performance. *Int J Eng Sci* 89:75–85
45. Zohdi TI, Kuypers FA (2006c) Modeling and rapid simulation of multiple red blood cell light scattering. *Proc R Soc Interface* 3(11):823–831